MATERIALS CHEMISTRY
FRONTIERS

RESEARCH ARTICLE

View Article Online
View Journal | View Issue

Cite this: *Mater. Chem. Front.*, 2021, **5**, 4327

Bromine anion mediated epitaxial growth of core–shell Pd@Ag towards efficient electrochemical CO_2 reduction†

Yinqiong Wu,‡ Jiachang Zeng,‡ Yang Yang, Zhaojie Li, Wenbiao Zhang, Dan Li and Qingsheng Gao *

Noble-metal core–shell nanostructures are promising electrocatalysts for CO_2 reduction thanks to their interfacial configurations which are beneficial for electrocatalytic kinetics, but are severely limited to a few couples that require tiny lattice mismatches (<3%) between two metals for classical epitaxial growth. Herein, non-classical epitaxial growth mediated by bromine anions (Br^-) is proposed to surmount the thermodynamic limitation of largely mismatched Ag and Pd lattices (5.012%), resulting in core–shell Pd@Ag cubes that are unavailable *via* conventional strategies. As evidenced, Br^- strongly bonded on the surface of Pd seeds serves as a buffer layer (possibly AgBr) to relieve interfacial strains and enable the epitaxial growth of Ag lattices. Due to interfacial electron-transfer, the engineered Ag sites enhance efficient CO_2 reduction to CO (faradaic efficiency ~85% at −0.8 V *vs.* RHE in 0.5 M $KHCO_3$), superior to the counterparts of Pd octahedrons, Ag nanoparticles and Pd–Ag nanoalloys. Providing new insights into the epitaxial growth of core–shell nanocrystals, this study is anticipated to inspire new design strategies for active and selective electrocatalysts.

Received 1st February 2021,
Accepted 7th April 2021

DOI: 10.1039/d1qm00169h

rsc.li/frontiers-materials

Introduction

The electrochemical synthesis of value-added feedback *via* carbon dioxide (CO_2) reduction is an appealing approach for the permanent storage of renewable electricity and closing the carbon neutral cycle.[1–4] There is high requirement for electrocatalysts to address the huge kinetic barriers and rationalize the reaction pathways.[5–7] For instance, noble-metal elements, *e.g.*, Pd, Au, and Ag, can efficiently reduce CO_2 to CO or formate, relying on surface atom arrangements and electronic configurations.[8–11] Further recent progress has been made on their core–shell nanostructures (*e.g.*, Pd@PdAu[12] and Au@Pd[13]) that effectively ameliorate intermediate bindings *via* either the strain effect induced by the structure or the electron transfer between two components.[14,15] Therefore, the rational construction of core–shell electrocatalysts with a particular emphasis on their interfacial interactions has attracted extensive attention.[16–19] Although kinetic control over nucleation and growth is important to avoid the formation of two individual nanocrystals,[20–22] the thermodynamics of epitaxial growth is a prerequisite for viable core–shell nanostructures. According to the layer-by-layer Frank–van der Merwe epitaxial growth model, a thermodynamic prerequisite is a small lattice mismatch (<3%) between core and shell elements,[23–25] which unfortunately limits the variety of core–shell electrocatalysts.

Thanks to the strong electronic interactions and the synergic enhancement between two metals, nanostructured Pd–Ag alloys have proved to have prominent electrocatalytic performances.[26–32] However, core–shell nanostructures of Pd@Ag have rarely been reported, because the great lattice mismatch (5.012%) between Pd and Ag restricts epitaxial growth.[20,33] Recently, binary PdAg alloys and Pd–H hydrides, instead of pure metal cores, were taken to synthesize PdAg@Ag octahedrons (Octs) and Pd@Ag nanosheets, respectively.[34,35] The alloying of Pd with Ag or H can effectively expand the lattices on the surface to alleviate the mismatch with Ag shells and thus reduce the interfacial strain, highlighting the mediated epitaxial growth by the surface modification of seeds. Considering that most nanocrystal seeds are surface bonded with capping agents (*e.g.*, oleylamine and halide anions) after wet-chemistry fabrication,[36,37] the residual adsorbents that are difficult to remove would play the role of middlemen to buffer the lattice mismatch between core and shell metals. However, relevant reports are scarce. An unexpected growth of Ag shells on

College of Chemistry and Materials Science, and Guangdong Provincial Key Laboratory of Functional Supramolecular Coordination Materials and Applications, Jinan University, Guangzhou 510632, P. R. China. E-mail: tqsgao@jnu.edu.cn

† Electronic supplementary information (ESI) available: Raw data of Pd@Ag cubes elemental mapping, XPS survey spectra of Pd@Ag cubes, TEM images of samples in control experiments, and LSV of Pd Octs, Ag nanoparticles, Pd–Ag nanoalloys and Pd@Ag in 0.5 M $KHCO_3$ saturated by N_2 and CO_2. See DOI: 10.1039/d1qm00169h

‡ These authors contribute equally to this work.

Pd cubes was always ascribed to the edge dislocation and stacking fault defects on Pd–Ag interfaces,[38] which, however, have not been sufficiently understood in the context of ignoring mediation by surface capping agents.

Here, a bromine anion (Br^-) mediated epitaxial growth of Ag shells on Pd Octs is proposed towards well-defined Pd@Ag core–shell cubes. Evidence is shown that the Br^- strongly bonded on the surface of Pd Octs benefits the formation of a buffer layer (possibly AgBr) to relieve the strain and mediate the further epitaxial growth of Ag lattices, resulting in core–shell Pd@Ag cubes enclosed predominantly by Ag{100} facets. The electron transfer from Ag to Pd is detectable, which will upshift the d-band centre of the engineered Ag sites, and thereby enhance the binding with *COOH, a key intermediate in CO_2 reduction.[39] Pd@Ag cubes afford prominent electrocatalytic performance for CO_2 reduction to CO with a high faradaic efficiency (FE) of ~85% at −0.8 V *vs.* RHE in 0.5 M $KHCO_3$, outperforming the counterparts of Pd Octs, Ag nanoparticles and Pd–Ag nanoalloys. Elucidating non-classical epitaxial growth of core–shell nanocrystals, this work will inspire the design of high-performance catalysts to be used in energy and environmental fields.

Experimental

Materials synthesis

Pd Octs as seeds for constructing Pd@Ag were synthesized according to previous reports.[37] 7 mL of a mixed solution containing 115 mmol L^{-1} cetyltrimethylammonium chloride (CTAC), 45 mmol L^{-1} citric acid and 50 mmol L^{-1} ascorbic acid (AA) was preheated to 100 °C in an oil bath under magnetic stirring (500 rpm). Quickly 4 mL of Na_2PdCl_4 (50 mmol L^{-1}) was injected into the above solution, and the reaction was allowed to proceed for 3 h. After cooling to room temperature, the Pd Octs were collected by centrifugation at 10 000 rpm for 10 min, and then washed with ultrapure water.

To fabricate core–shell Pd@Ag, 50 μL of Pd Octs solution (1 mg mL^{-1}) and 250 μL of cetyltrimethylammonium (CTAB, 20 mmol L^{-1}) were dispersed in 10 mL of ultrapure water and heated to 50 °C. The concentration of CTAB in solution is about 0.5 mmol L^{-1}. And then, 150 μL of $AgNO_3$ (10 mmol L^{-1}) was added into the above solution that was stood still for more 30 minutes. After injecting AA (450 μL, 0.1 mol L^{-1}), the solution was stirred at 50 °C for 6 h. Finally, Pd@Ag cubes were collected by centrifugation at 4500 rpm for 10 min.

Physical measurements

Transition electronic microscopy (TEM), energy dispersive spectroscopy (EDS) and the corresponding elemental mapping were collected on a JEOL 2100F instrument. X-ray diffraction (XRD) analysis was performed on Bruker D8 diffractometer using Cu Kα radiation (λ = 1.54056 Å). X-ray photoelectron spectroscopy (XPS) was conducted on Thermo Scientific (Escalab 250Xi), using C 1s (284.8 eV) as a reference.

Electrochemical measurements

All of the electrochemical measurements were conducted on an electrochemical workstation (CHI 760, Shanghai Chenhua), using a saturated calomel electrode (SCE) as the reference electrode, and a platinum (CV sweep) or a graphite electrode (CO_2RR) as the counter electrode. All potentials were converted to the RHE using the equation: E (*vs.* RHE) = E (*vs.* SCE) + 0.241 V + 0.0591 × pH. For the CV sweep to clean the Pd surface, 20 μL of Pd Octs (1 mg L^{-1}) solution were loaded onto a glassy carbon electrode (GCE) and tested in 0.5 M H_2SO_4. We also added 100 μL of CTAB (2×10^{-2} mol L^{-1}) to a Pd Octs solution (2 mL, 1 mg L^{-1}), 20 μL of which was then deposited onto a GCE for a control experiment. A CV scan between 0.1 and 1.2 V *vs.* RHE was taken to clean the surface of Pd, in which PdO formation/reduction and hydrogen/bisulfate adsorption/desorption could cause the removal of residual surfactants. For the CO_2RR performance, catalysts were loaded onto GCEs and tested in CO_2-saturated 0.5 M $KHCO_3$ solution. Typically, 0.76 mg (Pd@Ag : Vulcan XC-72R carbon black = 1 : 4) of catalyst and 15.0 μL of Nafion solution were dispersed in 360 μL of water–ethanol (volume ratio = 4 : 1) by sonication for 30 min to form a homogeneous ink. Then 20 μL of ink was loaded onto a GCE of 5 mm in diameter (geometric area: 0.196 cm^{-2}). The CO_2RR test was conducted in a gas-tight two-compartment electrochemical cell equipped with a piece of cation exchange membrane (Nafion 117, Sigma-Aldrich) as the compartment separator. Each compartment contained 45 mL of electrolyte. Before electrolysis, the electrolyte in the cathodic compartment was purged by CO_2 for at least 30 min. CO_2 was delivered into the cathodic compartment at a rate of 36 mL min^{-1} and the quantification of gaseous products was conducted on a gas chromatograph (GC). Gas-phase products were sampled every 30 min using high-purity nitrogen (N_2, 99.999%) as the carrier gas. The column effluent (separated gas mixtures) was first passed through a thermal conductivity detector (TCD) where hydrogen was quantified; then CO was converted to methane by passing through a methanizer and subsequently quantified by FID. According to the peak areas in GC, the partial current densities and FEs of CO and H_2 were calculated using the following equations (eqn (1)–(3)):

$$j_{CO} = \frac{\text{peak area of CO}}{\alpha} \times \text{flow rate} \times \frac{2F}{V_m} \times (\text{electrode area})^{-1} \quad (1)$$

$$j_{H_2} = \frac{\text{peak area of } H_2}{\beta} \times \text{flow rate} \times \frac{2F}{V_m} \times (\text{electrode area})^{-1} \quad (2)$$

$$\text{FE} = \frac{j_{CO} \text{ or } j_{H_2}}{j_{total}} \times 100\% \quad (3)$$

where α and β are the conversion factors for CO and H_2, respectively, based on the calibration of standard samples, V_m = 22.4 L mol^{-1}, and F is Faraday's constant (F = 96 485 C mol^{-1}).

Results and discussion

Pd Octs were used as the seeds for fabricating core–shell Pd@Ag. With an average edge length of 20 nm, Pd Octs specifically expose facets of {111} (Fig. 1a). The lattice fringe of 2.29 Å observed in high-resolution TEM (HR-TEM) corresponds to the (111) plane of an fcc Pd crystal. To further grow Ag on such Pd seeds, $AgNO_3$ was reduced by AA in the presence of CTAB, producing cubic nanocrystals with a size of about 40 nm (Fig. 1b). A closer observation shows clear octahedral outlines inside and moiré fringes due to overlapping lattices (Fig. 1c), indicating the successful growth of Ag on Pd Octs. The clear grain boundary between a Pd core and an Ag shell (Fig. 1d) is believed to accommodate the large lattice mismatch between the two metals.[38] Such Pd@Ag cubes mainly expose the Ag{100} facets on the shell, similar to previously reported Ag cubic nanocrystals.[20] As a capping agent, CTAB reduces the growth rate of the Ag{100}, stabilizes these facets, and guides the morphology, leading to the final formation of cubic shells. In addition, the corresponding elemental mapping confirms that a Pd octahedron (red) is inside the cube, and Ag (green) is distributed outside (Fig. 1e and f). We collected a series of EDS profiles from a few Pd@Ag cubes, and gained an average Pd/Ag atomic ratio of 0.33.

XRD and XPS investigations were further conducted to analyse Pd@Ag core–shell nanostructures. As depicted in the XRD patterns (Fig. 2a), Pd Octs exhibit the characteristic diffraction peaks indexed to the (111) and (200) planes of an fcc Pd crystal (JCPDS No. 46-1043). The main diffraction peaks of Pd@Ag cubes correspond to the (111) and (200) of Ag (JCPDS No. 04-0783), proving the effective reduction of Ag ions to crystallized Ag. In comparison with Pd Octs, the Pd(111) peak in Pd@Ag is obviously weakened, because the Pd core is wrapped in an Ag shell. Fig. 2b and c depict the XPS profiles of Pd and Ag, respectively, which clearly present varied chemical states owing to the core–shell structure. The Pd 3d profiles of Pd Octs can be deconvolved to three couples that are ascribed to metallic Pd^0, Pd^{2+} and $PdCl_2$ species, respectively. The presence of $PdCl_2$ is due to the high concentration of Cl^- required for fabrication. By contrast, the Pd 3d of Pd@Ag cubes can only be deconvolved to two couples associated with Pd^0 and Pd^{2+}. More importantly, the binding energies of Pd^0 $3d_{3/2}$ and $3d_{5/2}$ in Pd@Ag are 341.13 and 335.20 eV,[40] obviously lower than those of Pd Octs, which indicates the electron transfer from Ag to Pd according to their different electronegativities (Pd: 2.20 > Ag: 1.93). Accordingly, the presence of Ag is confirmed by the Ag 3d profile of Pd@Ag, which shows visible signals for Ag^+ species owing to the charge redistribution on Pd–Ag interfaces (Fig. 2c). Moreover, the atomic ratio of Pd to Ag on the surface of Pd@Ag is quantified as 1 : 18.4 by XPS survey spectra (Fig. S2, ESI†), agreeing with the core–shell structure.

The above characterizations have identified the successful formation of core–shell Pd@Ag that is, however, unavailable according to the Frank–van der Merwe epitaxial growth model. The lattice mismatch of Pd and Ag (5.012%) is larger than the threshold value of 3%, which makes it difficult for Ag to grow directly into a uniform single crystal shell on Pd. We found that adding CTAB is indispensable for epitaxial growth. As indicated by the TEM image (Fig. 3a), Pd Octs are well dispersed with clear octahedral outlines. When only $AgNO_3$ and AA are added into a clean solution of Pd Octs with heating, the Octs are severely agglomerated and no core–shell structure can be obtained (Fig. 3b). The residual Cl^- on the Pd surface, which was previously used as the capping agent to direct the formation of octahedral Pd seeds, will react with Ag^+ to produce AgCl colloids. In the presence of a suitable amount of CTAB, well-defined Pd@Ag cubes can be successfully achieved and the reaction solution turns yellow-brown owing to the surface plasmon resonance of nanostructured Ag (Fig. 3c).[41] This indicates the key role of Br^- for the non-classical epitaxial growth of Ag on Pd.

The functionality of Br^- was always implied by previously reported Pd@Ag cubes that were prepared with CTAB stabilized Pd seeds.[38] Although the formation of an Ag shell was ascribed to the edge dislocation and stacking fault defects on Pd–Ag interfaces, the mediation by the residual Br^- on the Pd surface deserved more concern. By contrast, the seeds used to fabricate Pd@Ag in this work are the Pd Octs with surface Cl^- adsorbates that are possibly exchanged with the Br^- derived from CTAB owing to its strong binding on Pd(111). In this regard, we employed a CV sweep in 0.5 M H_2SO_4 to remove the residual surfactants on the Pd surface, and CV was also used as a probe to examine the cleaning effect, inquiring into the difference between Cl^- and Br^- bindings on Pd Octs. At the beginning (Fig. 4a), Pd Octs show severely suppressed current peaks related to surface PdO formation/reduction and hydrogen/bisulfate adsorption/desorption, indicating Cl^- adsorbate remaining on Pd surface.[37] After 100 scans, the peak currents increase significantly, confirming the successful removal of adsorbents from Pd{111}. The unbroken crystal facets are also proved by the characteristic peaks of CVs which are consistent with the voltammetric features of single-crystal Pd electrodes.[42] In a control experiment,

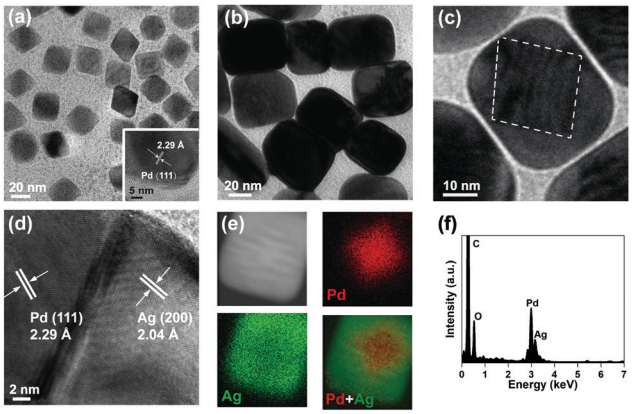

Fig. 1 Structural characterization of Pd Octs and Pd@Ag cubes. (a) TEM image of Pd Octs. (b and c) TEM and (d) HR-TEM images, (e) elemental mapping (raw data are displayed as Fig. S1, ESI†) and (f) the corresponding EDS profile of a Pd@Ag cube.

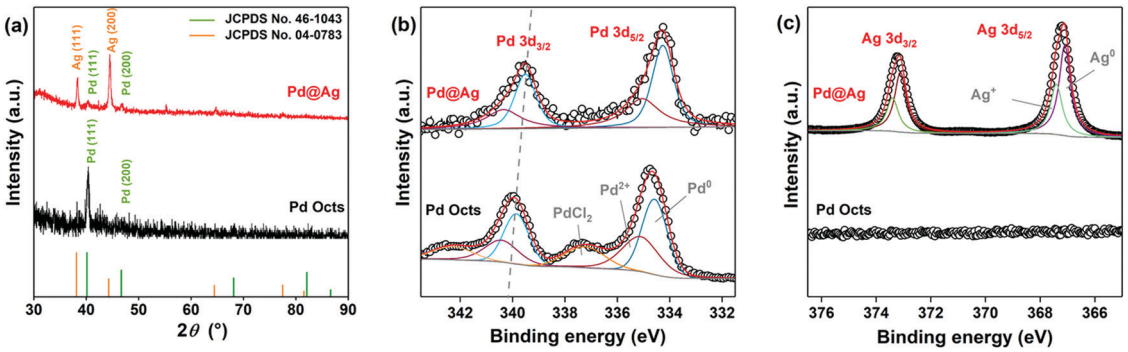

Fig. 2 (a) XRD patterns and XPS profiles of (b) Pd 3d and (c) Ag 3d of Pd@Ag cubes and Pd Octs.

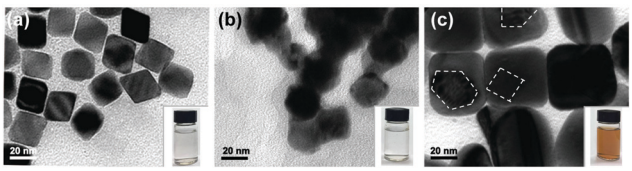

Fig. 3 TEM images of (a) Pd Octs, and samples obtained (b) without and (c) with CTAB. Insets correspond to the digital photos of the final solutions after preparation.

we added CTAB to Pd Octs, and the same CV sweep was performed (Fig. 4b). Even after 100 cycles, the current densities in CVs are still suppressed, without visible characteristic peaks associated with Pd(111). As indicated, the binding of Br^- is stronger than that of Cl^-, which drives the exchange of Cl^- by Br^- on the Pd Octs surface. The weak binding of Cl^- on the Pd surface can be further used to interpret the easy formation of AgCl precipitate when Cl^--capped Pd Octs are exposed to $AgNO_3$. The easily-exchangable Cl^- can desorb from the Pd surface to react with Ag^+. By contrast, Br^- strongly adsorbed on Pd Octs would direct the growth of the Ag shell. Further evidence is acquired from XPS analysis. Before CVs, there are the peaks for both Cl 2p and $PdCl_2$ in the XPS profile (Fig. 4c), but they both disappear after CVs, which proves once again that Cl^- has been removed from the Pd Octs surface. In comparison, after introducing CTAB to Pd Octs, the satellite peaks of $PdCl_2$ are significantly weakened. The signals for both Cl and $PdCl_2$ disappear after the sweep, while the peak of Br 3d still remains. It is confirmed that Br^- has replaced Cl^- and was strongly bonded on the surface of Pd seeds, which will benefit the formation of a buffer layer (possibly AgBr) between a Pd core and an Ag shell. The buffer layer relieves the strain and mediates the further epitaxial growth of Ag lattices,

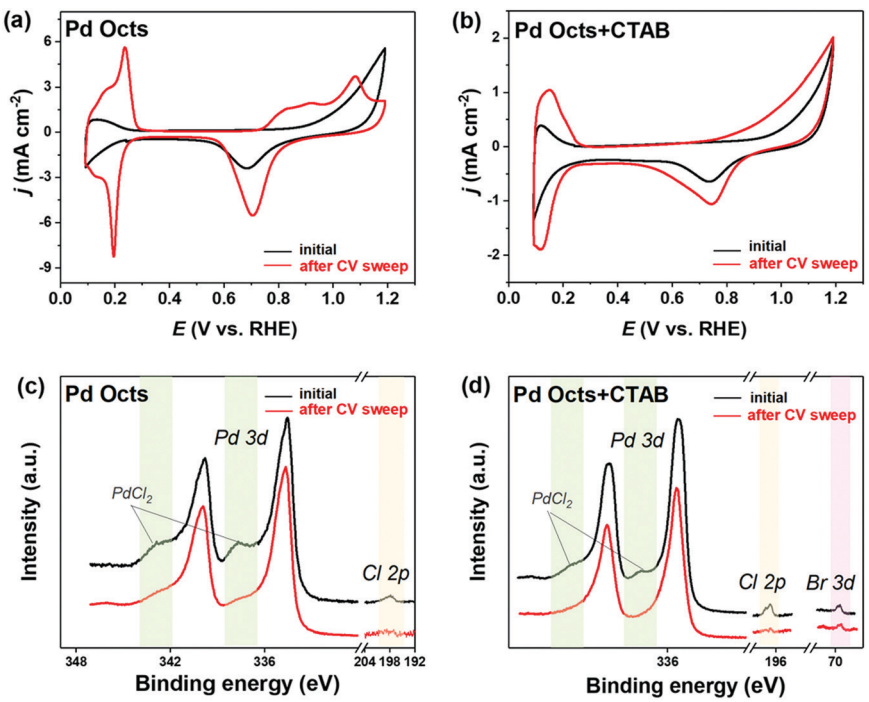

Fig. 4 Comparison of electrochemical surface cleaning for Pd Octs and Pd Octs with CTAB in 0.5 M H_2SO_4. (a and b) CVs and (c and d) XPS profiles of (a and c) Pd Octs and (b and d) Pd Octs with CTAB, before and after surface cleaning by CV sweeping.

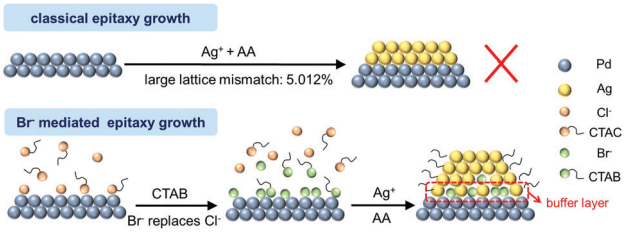

Fig. 5 Schematic illustration for the Br^- mediated epitaxial growth towards Pd@Ag cubes.

resulting in a non-classical manner of epitaxial growth for constructing core–shell Pd@Ag.

Such epitaxial growth depends highly on the surface Br^- adsorbent. When excessive CTAB (1.0 mmol L^{-1}) is introduced, there is a considerable amount of Br^- and CTA^+ in solution that unfortunately favours the formation of individual Ag nanoparticles, rather than epitaxial growth on Pd seeds (Fig. S3, ESI†). In the meantime, the CTA^+ long-chain is also important to produce well-dispersed core–shell nanocrystals, because it can prevent the agglomeration of nanocrystals.[43] When KBr is used to prepare Pd@Ag, only white colloid AgBr precipitates are obtained, which would disturb the growth of Pd@Ag (Fig. S4, ESI†). In addition, the surfactant of CTAB will direct the growth of Ag crystals towards cubic nanostructures mainly exposing {100} facets.

On the basis of the above analysis, we propose a mechanism for the unexpected manner of epitaxial growth towards core–shell Pd@Ag (Fig. 5). When CTAB is introduced into the reaction, the exchange of Cl^- adsorbents by Br^- on the surface of Pd seeds is enabled owing to the stronger binding of the latter. To keep the surface charge balance, CTA^+ long chains will wrap up the seeds and stabilize them for further reactions. Owing to the low solubility product constant of AgBr (5.0×10^{-13}), Ag^+ will be deposited on the Pd surface, possibly in the form of AgBr, resulting in a buffer layer to alleviate the mismatch and thus reduce the interfacial strains between a Pd core and an Ag shell. Thereby, this non-classical epitaxial growth of Ag on Pd is achieved *via* key mediation by Br^-, which is only available on a surface that can effectively adsorb and stabilize Br^-.

Noble-metal core–shell nanostructures can effectively ameliorate intermediate bindings and then cut down reaction energy barriers for CO_2RR.[44,45] Before CO_2RR tests, Pd Octs and Pd@Ag cubes were examined by CVs (Fig. 6a). Pd Octs show obvious characteristic peaks that disappear when Pd is coated with Ag. This proves the formation of a core–shell structure that exposes an Ag shell outside Pd@Ag. The CO_2RR activity of carbon (Vulcan XC-72R) supported Pd@Ag cubes, Ag nanoparticles, Pd–Ag nanoalloys (Pd/Ag = 0.33), and Pd Octs was then investigated in an H-cell with CO_2-saturated 0.5 M $KHCO_3$ aqueous solution. All the samples afford a higher current density with CO_2 saturation than the cases saturated with N_2, indicating the reduction of CO_2 (Fig. S5, ESI†). Fig. 6b displays the linear sweeping voltammetry (LSV) curves, in which Pd@Ag shows the highest current density and the lowest overpotential. Over a wide potential range from −0.9 V to −0.6 V (*vs.* RHE), Pd@Ag cubes achieve a high CO FE of 85%, which is better than the counterparts (Fig. 6c). Furthermore, a durability experiment over Pd@Ag was investigated at −0.8 V for 24 h. It affords stable current output and CO FE (Fig. 6d), confirming the satisfactory long-term durability of this core–shell electrocatalyst. Accordingly, TEM observation confirms the well-maintained core–shell nanostructures of Pd@Ag after a long-term test (inset of Fig. 6d). Regarding the CO_2 reduction occurring on the catalyst surface, we can deduce that the Ag shell as the

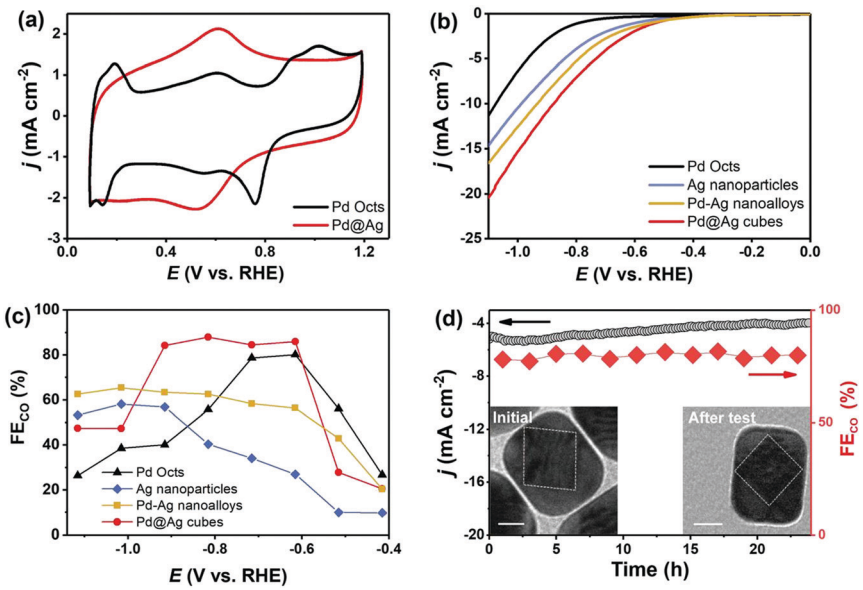

Fig. 6 CO_2RR performance in CO_2-saturated 0.5 M $KHCO_3$. (a) CV curves without bubbling CO_2; (b) polarization curves; (c) FE of CO at various applied potentials; (d) long-term *i*–*t* curve and CO FE, along with TEM images before and after electrolysis (scale bar: 20 nm).

electrocatalytically active sites is effectively engineered by the Pd core *via* strong electronic interactions. The proven electron transfer from Ag to Pd by XPS (Fig. 2) leads to the upshifted d-band centre of Ag, and consequently enhances the binding with *COOH intermediates. Such enhancement can overcome the high energy barrier of generating *COOH that is typically considered as the potential determining step for CO_2RR over Ag catalysts.[31,46] It is noteworthy that compressive strain of shell Ag lattices is possible,[18] but this effect would be negligible due to the thick Ag shell. Therefore, the interfacial interactions in Pd@Ag cubes, mainly electronic effects, account for the obviously boosted CO_2RR performance.

Conclusions

In summary, a Br^- mediated epitaxial growth is successfully introduced to synthesize Pd@Ag core–shell cubes with Pd Octs as the seeds. Control experiments and characterizations show that Br^- can be adsorbed on the Pd surface and form an AgBr buffer layer to effectively overcome the large lattice mismatch between Pd and Ag. As a result, non-classical epitaxial growth is enabled towards core–shell nanostructures that are unavailable *via* conventional strategies. Such unique Pd@Ag core–shell nanostructures prove to have obviously improved CO_2RR performance owing to the engineered Ag sites *via* interfacial electron-transfer. In CO_2-saturated 0.5 M $KHCO_3$, they afford better activity and higher efficiency (CO FE of 85% at −0.8 V *vs.* RHE) than Pd Octs, Ag nanoparticles or even Pd–Ag nanoalloys. Providing a new understanding of the epitaxial growth of core–shell nanocrystals, this work will inspire the exploitation of high-performance electrocatalysts to be used in energy and environmental fields.

Conflicts of interest

There are no conflicts to declare.

Acknowledgements

The authors appreciate the financial support from the National Natural Science Foundation of China (grant no.: 21773093), Guangdong Natural Science Foundation (2021A1515012351) and China Postdoctoral Science Foundation funded project (grant no.: 2020M673056).

References

1 X. Tan, C. Yu, Y. Ren, S. Cui, W. Li and J. Qiu, Recent advances in innovative strategies for the CO_2 electroreduction reaction, *Energy Environ. Sci.*, 2021, **14**, 765–780.
2 P. De Luna, C. Hahn, D. Higgins, S. A. Jaffer, T. F. Jaramillo and E. H. Sargent, What would it take for renewably powered electrosynthesis to displace petrochemical processes?, *Science*, 2019, **364**, eaav3506.
3 D. Gao, R. M. Aran-Ais, H. S. Jeon and B. Roldan Cuenya, Rational catalyst and electrolyte design for CO_2 electroreduction towards multicarbon products, *Nat. Catal.*, 2019, **2**, 198–210.
4 J. Qiao, Y. Liu, F. Hong and J. Zhang, A review of catalysts for the electroreduction of carbon dioxide to produce low-carbon fuels, *Chem. Soc. Rev.*, 2014, **43**, 631–675.
5 M. B. Ross, P. De Luna, Y. Li, C.-T. Dinh, D. Kim, P. Yang and E. H. Sargent, Designing materials for electrochemical carbon dioxide recycling, *Nat. Catal.*, 2019, **2**, 648–658.
6 Y. Zheng, A. Vasileff, X. Zhou, Y. Jiao, M. Jaroniec and S.-Z. Qiao, Understanding the roadmap for electrochemical reduction of CO_2 to multi-carbon oxygenates and hydrocarbons on copper-based catalysts, *J. Am. Chem. Soc.*, 2019, **141**, 7646–7659.
7 S. Nitopi, E. Bertheussen, S. B. Scott, X. Liu, A. K. Engstfeld, S. Horch, B. Seger, I. E. L. Stephens, K. Chan, C. Hahn, J. K. Nørskov, T. F. Jaramillo and I. Chorkendorff, Progress and perspectives of electrochemical CO_2 reduction on copper in aqueous electrolyte, *Chem. Rev.*, 2019, **119**, 7610–7672.
8 J. Wu, Y. Huang, W. Ye and Y. Li, CO_2 reduction: from the electrochemical to photochemical approach, *Adv. Sci.*, 2017, **4**, 1700194.
9 A. D. Handoko, F. Wei, B. S. Yeo and Z. W. Seh, Understanding heterogeneous electrocatalytic carbon dioxide reduction through operando techniques, *Nat. Catal.*, 2018, **1**, 922–934.
10 D. Gao, H. Zhou, F. Cai, J. Wang, G. Wang and X. Bao, Pd-containing nanostructures for electrochemical CO_2 reduction reaction, *ACS Catal.*, 2018, **8**, 1510–1519.
11 S. Thota, Y. Wang and J. Zhao, Colloidal Au-Cu alloy nanoparticles: synthesis, optical properties and applications, *Mater. Chem. Front.*, 2018, **2**, 1074–1089.
12 X. Yuan, L. Zhang, L. Li, H. Dong, S. Chen, W. Zhu, C. Hu, W. Deng, Z.-J. Zhao and J. Gong, Ultrathin Pd–Au shells with controllable alloying degree on Pd nanocubes toward carbon dioxide reduction, *J. Am. Chem. Soc.*, 2019, **141**, 4791–4794.
13 S. Zhu, X. Qin, Q. Wang, T. Li, R. Tao, M. Gu and M. Shao, Composition-dependent CO_2 electrochemical reduction activity and selectivity on Au–Pd core–shell nanoparticles, *J. Mater. Chem. A*, 2019, **7**, 16954–16961.
14 C. Xie, Z. Niu, D. Kim, M. Li and P. Yang, Surface and interface control in nanoparticle catalysis, *Chem. Rev.*, 2019, **120**, 1184–1249.
15 X. Yin, L. Yang and Q. Gao, Core–shell nanostructured electrocatalysts for water splitting, *Nanoscale*, 2020, **12**, 15944–15969.
16 Y. W. Lee, M. Kim, Z. H. Kim and S. W. Han, One-step synthesis of Au@Pd core−shell nanooctahedron, *J. Am. Chem. Soc.*, 2009, **131**, 17036–17037.
17 J. Gu, Y.-W. Zhang and F. Tao, Shape control of bimetallic nanocatalysts through well-designed colloidal chemistry approaches, *Chem. Soc. Rev.*, 2012, **41**, 8050–8065.
18 M. Luo and S. Guo, Strain-controlled electrocatalysis on multimetallic nanomaterials, *Nat. Rev. Mater.*, 2017, **2**, 17059.

19 Y. Ge, Z. Huang, C. Ling, B. Chen, G. Liu, M. Zhou, J. Liu, X. Zhang, H. Cheng, G. Liu, Y. Du, C.-J. Sun, C. Tan, J. Huang, P. Yin, Z. Fan, Y. Chen, N. Yang and H. Zhang, Phase-selective epitaxial growth of heterophase nanostructures on unconventional 2H-Pd nanoparticles, *J. Am. Chem. Soc.*, 2020, **142**, 18971–18980.

20 J. Zeng, C. Zhu, J. Tao, M. Jin, H. Zhang, Z.-Y. Li, Y. Zhu and Y. Xia, Controlling the nucleation and growth of silver on palladium nanocubes by manipulating the reaction kinetics, *Angew. Chem., Int. Ed.*, 2012, **51**, 2354–2358.

21 C. Fang, T. Bi, Q. Ding, Z. Cui, N. Yu, X. Xu and B. Geng, High-density Pd nanorod arrays on Au nanocrystals for high-performance ethanol electrooxidation, *ACS Appl. Mater. Interfaces*, 2019, **11**, 20117–20124.

22 C. Fang, J. Zhao, R. Jiang, J. Wang, G. Zhao and B. Geng, Engineering of hollow PdPt nanocrystals via reduction kinetic control for their superior electrocatalytic performances, *ACS Appl. Mater. Interfaces*, 2018, **10**, 29543–29551.

23 C. Zhu, J. Zeng, J. Tao, M. C. Johnson, I. Schmidt-Krey, L. Blubaugh, Y. Zhu, Z. Gu and Y. Xia, Kinetically controlled overgrowth of Ag or Au on Pd nanocrystal seeds: from hybrid dimers to nonconcentric and concentric bimetallic nanocrystals, *J. Am. Chem. Soc.*, 2012, **134**, 15822–15831.

24 E. Bauer and J. H. van der Merwe, Structure and growth of crystalline superlattices: From monolayer to superlattice, *Phys. Rev. B: Condens. Matter Mater. Phys.*, 1986, **33**, 3657–3671.

25 K. A. Lozovoy, A. G. Korotaev, A. P. Kokhanenko, V. V. Dirko and A. V. Voitsekhovskii, Kinetics of epitaxial formation of nanostructures by Frank–van der Merwe, Volmer–Weber and Stranski–Krastanow growth modes, *Surf. Coat. Technol.*, 2020, **384**, 125289.

26 Y. Zhou, N. Han and Y. Li, Recent progress on Pd-based nanomaterials for electrochemical CO_2 reduction, *Acta Phys.-Chim. Sin.*, 2020, **36**, 2001041.

27 M. Cui, G. Johnson, Z. Zhang, S. Li, S. Hwang, X. Zhang and S. Zhang, AgPd nanoparticles for electrocatalytic CO_2 reduction: bimetallic composition-dependent ligand and ensemble effects, *Nanoscale*, 2020, **12**, 14068–14075.

28 J. H. Lee, S. Kattel, Z. Jiang, Z. Xie, S. Yao, B. M. Tackett, W. Xu, N. S. Marinkovic and J. G. Chen, Tuning the activity and selectivity of electroreduction of CO_2 to synthesis gas using bimetallic catalysts, *Nat. Commun.*, 2019, **10**, 3724.

29 M. Nazemi, P. Ou, A. Alabbady, L. Soule, A. Liu, J. Song, T. A. Sulchek, M. Liu and M. A. El-Sayed, Electrosynthesis of ammonia using porous bimetallic Pd-Ag nanocatalysts in liquid- and gas-phase systems, *ACS Catal.*, 2020, **10**, 10197–10206.

30 M. Yang, X. Lao, J. Sun, N. Ma, S. Wang, W. Ye and P. Guo, Assembly of bimetallic PdAg nanosheets and their enhanced electrocatalytic activity toward ethanol oxidation, *Langmuir*, 2020, **36**, 11094–11101.

31 J. Zeng, W. Zhang, Y. Yang, D. Li, X. Yu and Q. Gao, Pd-Ag alloy electrocatalysts for CO_2 reduction: Composition tuning to break the scaling relationship, *ACS Appl. Mater. Interfaces*, 2019, **11**, 33074–33081.

32 C. Fang, J. Zhao, G. Zhao, L. Kuai and B. Geng, Simultaneous tunable structure and composition of PtAg alloyed nanocrystals as superior catalysts, *Nanoscale*, 2016, **8**, 14971–14978.

33 C. Zhu, J. Zeng, J. Tao, M. C. Johnson, I. Schmidt-Krey, L. Blubaugh, Y. Zhu, Z. Gu and Y. Xia, Kinetically controlled overgrowth of Ag or Au on Pd nanocrystal seeds: from hybrid dimers to nonconcentric and concentric bimetallic nanocrystals, *J. Am. Chem. Soc.*, 2012, **134**, 15822–15831.

34 B.-S. Choi, J. Song, M. Song, B. S. Goo, Y. W. Lee, Y. Kim, H. Yang and S. W. Han, Core–shell engineering of Pd–Ag bimetallic catalysts for efficient hydrogen production from formic acid decomposition, *ACS Catal.*, 2018, **9**, 819–826.

35 X. Wang, B. Wu, G. Chen, Y. Zhao, P. Liu, Y. Dai and N. Zheng, A hydride-induced-reduction strategy for fabricating palladium-based core–shell bimetallic nanocrystals, *Nanoscale*, 2014, **6**, 6798–6804.

36 X.-Y. Ma, Y. Chen, H. Wang, Q.-X. Li, W.-F. Lin and W.-B. Cai, Electrocatalytic oxidation of ethanol and ethylene glycol on cubic, octahedral and rhombic dodecahedral palladium nanocrystals, *Chem. Commun.*, 2018, **54**, 2562–2565.

37 Y. Yang, J. Zeng, Y. Shu and Q. Gao, Revealing facet effects of palladium nanocrystals on electrochemical biosensing, *ACS Appl. Mater. Interfaces*, 2020, **12**, 15622–15630.

38 J. Gong, F. Zhou, Z. Li and Z. Tang, Controlled synthesis of non-epitaxially grown Pd@Ag core–shell nanocrystals of interesting optical performance, *Chem. Commun.*, 2013, **49**, 4379–4381.

39 A. Vasileff, C. Xu, Y. Jiao, Y. Zheng and S.-Z. Qiao, Surface and interface engineering in copper-based bimetallic materials for selective CO_2 electroreduction, *Chem*, 2018, **4**, 1809–1831.

40 W. Huang, X. Kang, C. Xu, J. Zhou, J. Deng, Y. Li and S. Cheng, 2D PdAg alloy nanodendrites for enhanced ethanol electroxidation, *Adv. Mater.*, 2018, **30**, 1706962.

41 J. He, S. Li, D. Lyu, D. Zhang, X. Wu and Q.-H. Xu, Aggregation induced emission enhancement by plasmon coupling of noble metal nanoparticles, *Mater. Chem. Front.*, 2019, **3**, 2421–2427.

42 M. Hara, U. Linke and T. Wandlowski, Preparation and electrochemical characterization of palladium single crystal electrodes in 0.1 M H_2SO_4 and $HClO_4$: Part I. Low-index phases, *Electrochim. Acta*, 2007, **52**, 5733–5748.

43 F. Wu, W. Wang, Z. Xu and F. Li, Bromide (Br)-based synthesis of Ag nanocubes with high-yield, *Sci. Rep.*, 2015, **5**, 10772.

44 J. Fan, H. Du, Y. Zhao, Q. Wang, Y. Liu, D. Li and J. Feng, Recent progress on rational design of bimetallic Pd based catalysts and their advanced catalysis, *ACS Catal.*, 2020, **10**, 13560–13583.

45 S. Das, J. Perez-Ramirez, J. Gong, N. Dewangan, K. Hidajat, B. C. Gates and S. Kawi, Core-shell structured catalysts for thermocatalytic, photocatalytic, and electrocatalytic conversion of CO_2, *Chem. Soc. Rev.*, 2020, **49**, 2937–3004.

46 S. Liu, H. Tao, L. Zeng, Q. Liu, Z. Xu, Q. Liu and J.-L. Luo, Shape-dependent electrocatalytic reduction of CO_2 to CO on triangular silver nanoplates, *J. Am. Chem. Soc.*, 2017, **139**, 2160–2163.